



NRL/FR/6840--95-9783

Recent Developments in Inductive Output Amplifiers

M.A. KODIS
K.L. JENSEN
E.G. ZAIDMAN

*Vacuum Electronics Branch
Electronics Science and Technology Division*

B. GOPLIN
D.N. SMITHE

*Mission Research Corporation
Newington, VA*

October 12, 1995

19951025 041

Approved for public release; distribution unlimited.

DTIC QUALITY INSPECTED 8



REPORT DOCUMENTATION PAGE			Form Approved OMB No. 0704-0188	
Public reporting burden for this collection of information is estimated to average 1 hour per response, including the time for reviewing instructions, searching existing data sources, gathering and maintaining the data needed, and completing and reviewing the collection of information. Send comments regarding this burden estimate or any other aspect of this collection of information, including suggestions for reducing this burden, to Washington Headquarters Services, Directorate for Information Operations and Reports, 1215 Jefferson Davis Highway, Suite 1204, Arlington, VA 22202-4302, and to the Office of Management and Budget, Paperwork Reduction Project (0704-0188), Washington, DC 20503.				
1. AGENCY USE ONLY (Leave Blank)		2. REPORT DATE October 12, 1995		3. REPORT TYPE AND DATES COVERED
4. TITLE AND SUBTITLE Recent Developments in Inductive Output Amplifiers			5. FUNDING NUMBERS PE — 0602234N ONR — R534R54	
6. AUTHOR(S) M.A. Kodis, K.L. Jensen, E.G. Zaidman, B. Goplen* and D.N. Smithe*				
7. PERFORMING ORGANIZATION NAME(S) AND ADDRESS(ES) Naval Research Laboratory Washington, DC 20375-5320			8. PERFORMING ORGANIZATION REPORT NUMBER NRL/FR/6840--95-9783	
9. SPONSORING/MONITORING AGENCY NAME(S) AND ADDRESS(ES) Office of Naval Research Arlington, VA 22217-5000			10. SPONSORING/MONITORING AGENCY REPORT NUMBER	
11. SUPPLEMENTARY NOTES *Mission Research Corporation, Newington, VA 22122				
12a. DISTRIBUTION/AVAILABILITY STATEMENT Approved for public release; distribution unlimited.			12b. DISTRIBUTION CODE	
13. ABSTRACT (Maximum 200 words) An inductive output amplifier is an RF device in which an emission-gated electron beam induces RF fields in an output circuit by means of displacement currents, not convection current. Emission-gated electron beams experience strong interactions when traversing a resonant or synchronous electromagnetic field, and this strong interaction is responsible for both the interesting nonlinear physics and the attractive efficiency and compactness of emission-gated amplifiers. Field emission cathodes, due to their extremely low electron transit time and high transconductance, offer the opportunity to extend the advantages of spatiotemporal modulation into C and X bands. This paper presents design criteria for the joint optimization of the field emission array structure and the RF input and output circuits of inductive output amplifiers. We find that while output circuits yielding net efficiencies of 50% or greater are well within the state of the art, the gain is likely to be moderate (10 to 20 dB). With today's FEA performance, a desirable operating regime is achievable, yielding a new class of compact, highly efficient, and moderate-gain power booster amplifiers.				
14. SUBJECT TERMS Field emission arrays Klystrode Fowler-Nordheim Twystrode Inductive output amplifiers Simulation			15. NUMBER OF PAGES 28	
			16. PRICE CODE	
17. SECURITY CLASSIFICATION OF REPORT UNCLASSIFIED		18. SECURITY CLASSIFICATION OF THIS PAGE UNCLASSIFIED		19. SECURITY CLASSIFICATION OF ABSTRACT UNCLASSIFIED
20. LIMITATION OF ABSTRACT UL				

CONTENTS

1. INTRODUCTION		1
2. EXPERIMENTAL STATUS OF IOAs		2
3. CATHODE REQUIREMENTS		4
3.1. Transit Time		4
3.2. Transconductance		6
3.3. Capacitance		6
3.4. Gain		7
3.5. Current Density		8
4. CATHODE OF CHOICE—FEAs		11
4.1 Current vs Gate Voltage Modeling		11
4.2 Gated FEA Figure of Merit		16
5. EFFICIENCY		17
5.1. Performance Criteria		17
5.2. Klystrode		17
5.3. Twystrode		18
5.4. Further Development Under Way		20
6. EXAMPLES		20
7. CONCLUSIONS		23
ACKNOWLEDGMENTS		23
REFERENCES		23

Accession For		
NTIS	CRA&I	<input checked="" type="checkbox"/>
DTIC	TAB	<input type="checkbox"/>
Unannounced		<input type="checkbox"/>
Justification _____		
By _____		
Distribution / _____		
Availability Codes		
Dist	Avail and/or Special	
A-1		

INDUCTIVE OUTPUT AMPLIFIERS

1. INTRODUCTION

Inductive output amplifiers (IOA) use an emission-gated beam in which the emission current density of the cathode is a periodic function of time and/or position on the cathode surface. This class of devices is characterized by the following: (1) the beam is fully modulated before acceleration to cathode potential; (2) velocity dispersion in the beam is minimized; (3) there is no drift space for the purpose of converting velocity modulation into density modulation; and (4) the rf output electrode(s) and the beam collection electrodes are separate and distinct. Superior efficiency in converting beam power to circuit wave power results from the minimal velocity dispersion and from the separation of the RF output and beam collection electrodes. Compactness and specific power improvements follow from the absence of a drift space and its associated length of magnet. Although emission gating of electron beams offers clear advantages in efficiency and compactness, it makes stringent demands of the cathode structures where the gating occurs.

Field emission arrays (FEAs) have long been recognized as promising replacements for thermionic emitters in vacuum devices due to their instant turn-on and high current density capabilities. Recent improvements in gated FEA technology provide a new alternative to gridded thermionic electron beam sources [1] at frequencies above UHF. However, this new opportunity is subject to the integration of FEA technology into the vacuum tube environment.[2] Inductive output amplifiers require modulation of the emission current from the ultrasharp tips (radius of curvature $\leq 100 \text{ \AA}$) by means of voltage applied to the gate electrodes. Because the gate is generally coplanar with the emitter tips, the transit time of the FEA is orders of magnitude lower compared to thermionic cathodes where the gate plane is on the order of $500 \text{ }\mu\text{m}$ from the cathode surface. Superior transconductance is anticipated due to the exponential voltage dependence of the field emission current compared to the $V^{3/2}$ dependence typically seen in thermionic cathodes. The potential of gated FEA cathodes for low transit time and high transconductance, added to instant turn-on and high current density, has generated considerable interest in developing an FEA cathode for inclusion into a twystrode or klystrode amplifier.

With the notable exceptions of the Varian klystrode and the Naval Research Laboratory (NRL) twystrode experiments (to be discussed in Section 2), there has been little development of thermionic IOAs in recent years and no application of gated field emission arrays in IOAs. In the absence of practical experience with gated field-emission IOAs covering a significant range of operating conditions, there is need for a systematic procedure to evaluate components, such as input and output circuits and the FEAs, for their individual merit and combined ability to meet a given set of amplifier specifications. To develop this procedure, we have (1) chosen figures of merit for the amplifier performance, such as gain and efficiency; (2) analyzed the individual components using tools developed through research over the last decade; (3) devised scaling laws for the performance of the components; (4) linked the scaling laws to predict amplifier performance; and (5) mutually optimized the component specifications to meet the amplifier specifications. While the input circuit affects gain and the output circuit affects efficiency, the FEA strongly affects both gain and efficiency. In this paper, we derive the FEA characteristics required for high performance.

2. EXPERIMENTAL STATUS OF IOAs

A. V. Haeff [3,4,5] provided the first description of a premodulated electron beam combined with a nonintercepting output circuit, which he called the inductive output amplifier. He built and tested a developmental tube consisting of a grid-controlled thermionic cathode, cavity output circuit, and depressed collector, and obtained 10 dB gain and 25% net efficiency at 500 MHz. He also noted that the electron transit time in the grid-cathode gap limits the highest frequency of operation. This approach—contemporary with the initial development of velocity-modulated klystrons—was dropped as the advantage of velocity modulation in producing high gain became apparent. The first report of a prebunched beam passed through a traveling-wave output circuit appeared more than two decades later. This experiment, by A. J. Lichtenberg [6], employed both a gridded cathode for temporal modulation of the current and an inductively tuned cavity for velocity modulation of the electrons. The output end of the helix terminated in an internal tapered load rather than a vacuum window; power measurements were made by a traveling probe. Current modulation increased the single-pass efficiency from 20% to 40%, with the best efficiency observed when the input power to the helix was just sufficient to counteract longitudinal space-charge debunching forces in the beam. A second experiment with an output window revealed the considerable difficulty of impedance-matching the output in the presence of the prebunched beam. The development of pyrolytic graphite [7,8,9] provided a new alternative to metal grids, enabling fabrication of grid structures with superior dimensional stability at high temperatures and good thermal and electrical conductivity. Such highly refractory grids could be placed very close to the surface of large cathodes, thus allowing development of high-power gridded thermionic cathodes with electron transit times under 1 nano-second. In the 1970s, commercial demand for efficient, high-power amplifiers drove the development of the Varian klystrode for UHF television transmitter service [10,11]. The klystrode is particularly well suited to efficient amplification of television signals because it combines the efficient output-coupling cavity of a klystron with Class C operation; when the signal amplitude is small, the average beam power drops proportionately. In the late 80s, Varian built and tested a very-high-power klystrode as a linear accelerator driver. Power output of 500 kW was achieved [12].

The Navy's need for compact and efficient power amplifiers suitable for mobile platforms has motivated a combined experimental, simulation, and analytical study of twystrodes [13,14], or IOAs with traveling-wave output circuits. The experimental amplifier development program at NRL has provided extensive information on the coupling of emission-gated electron beams to helical output circuits, including the tradeoffs among gain, efficiency and compactness. The results of the experiments have been used to verify simulations run with the $2\frac{1}{2}$ D particle-in-cell code MAGIC [15], with the objective of developing a predictive design capability for twystrode amplifiers.

The initial twystrode experiments used a gridded thermionic gun and a UHF input circuit manufactured by Varian, chosen as the most robust and reliable available technology. The electron beam modulation is continuously variable over current ratios (average to peak) of $0.2 < I_a/I_p < 1.0$ (or from current emission during only one-fourth of each rf cycle to a dc, unmodulated beam). The tightness of the bunching is limited by the available drive power, not by space-charge expansion or thermal velocity effects. The output circuits are tape helices, lightly loaded with vanes for moderate dispersion and carrying 2 dB of carbon attenuation near the input window for stability. Because the input circuit is narrowband, all the measurements have been made at a frequency of 487 MHz; the wideband, low-dispersion output circuit is used because its reduced stability and coupling impedance make it a rigorous test of the prospects for wideband twystrodes when wideband cathodes become available.

To date, three twystrodes have been studied, with circuits 1, 2.25, and 3.25 wavelengths long. Figure 1 shows the 2.25-wavelength helix. The 3.25-wavelength circuit was unstable due to impedance mismatch at the output windows; fortunately, simulation studies subsequent to its initial design showed that it was too long for maximum efficiency. For the extremely short, one-wavelength-long helix, the efficiency improves for increasing beam current and decreasing bunch width. For the 2.25 wavelength helix, the efficiency improves monotonically with current but an optimum bunch width is observed, which also increases with current. This is consistent with saturation occurring in a shorter distance for higher current and narrower bunch width. The agreement with simulation is excellent; Fig. 2 shows simulations of growth and saturation with data from both experiments. Note that the length of circuit to saturation decreases as the bunch width decreases.

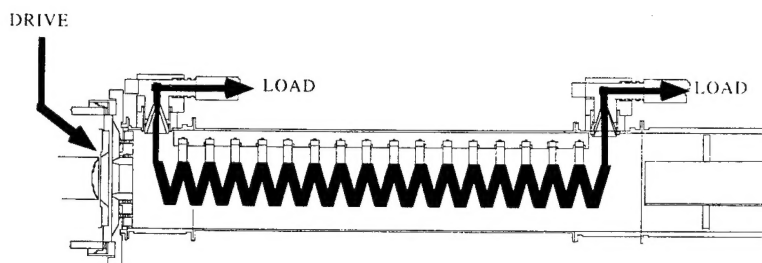


Fig. 1 —Experimental twystrode circuit

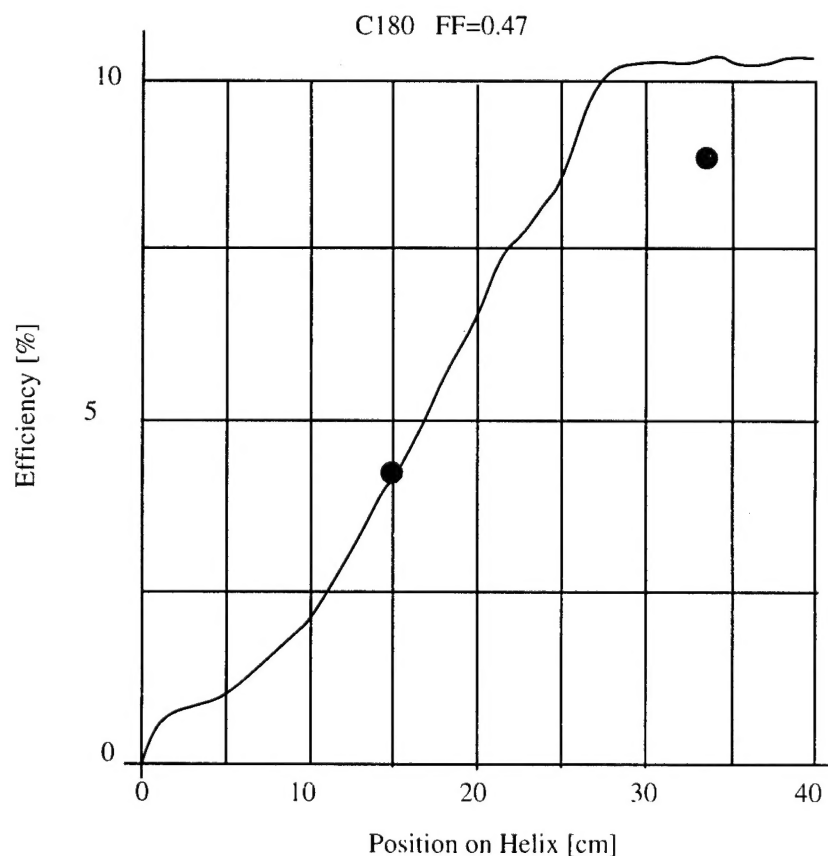


Fig. 2 — Simulations of circuit power vs position with experimental data points at 1 wavelength and 2.25 wavelengths

These experiments have shown that space-charge debunching of the beam is not significant; we hypothesize that the circuit field grows up rapidly enough to confine the beam. The saturation efficiency is limited by loss of synchronism between the bunches and the circuit, not by dispersion of the bunches. Accordingly the simulation effort was broadened to include velocity-tapered helices [16]. A quadratic taper of the helix pitch was assumed and the initial, half-way, and final phase velocities adjusted for maximum efficiency. A radically tapered helix pitch with an exit velocity one-third of the initial velocity converted over 45% of the beam power to the fundamental harmonic frequency in these simulations. The efficiency vs distance for this case is shown in Fig. 3(a), which gives the ratio of the power in the fundamental harmonic circuit wave to the initial beam power. Figure 3(b) illustrates the corresponding phase space (axial momentum of beam particles vs axial position); a cross-section of the beam is shown in Fig. 3(c). The need to prevent electron reversal ultimately limits energy extraction from the beam. An experimental helix has been constructed to this design and is in cold test.

This research, using commercially available technology, has demonstrated that strong coupling exists between an emission-gated electron beam and a traveling-wave circuit, converting beam power to circuit power at rates up to 20% per wavelength. Practical twystrodes are expected to be 5 to 10 times shorter and double the efficiency of traveling wave tubes of comparable frequencies. Extensions of the experimental program with field emission cathodes are under way at Varian and at NRL. The design process for these experiments will be discussed in Section 4.

3. CATHODE REQUIREMENTS

The key to the performance advantages of IOAs is emission gating of the electron beam at the cathode surface, before acceleration to anode potential. The cathode assembly that performs this modulation is, for most applications, either an old technology pushed to its fundamental limitations (i.e., gridded thermionic cathodes) or a new technology pushed to its present limits of performance (i.e., FEAs or laser-driven photocathodes). The critical measures of the performance of any emission-gated cathode are low transit time, high transconductance, and a low input power for the required beam modulation. In addition, the current density should be neither too low nor too high for good beam optics. Each of these factors are reviewed below and figures of merit are used to compare the different technologies.

3.1. Transit Time

It is a well known rule of design for triodes, tetrodes, etc., that the electron transit time must be less than about one-third of the period to avoid excessive loading of the input cavity and loss of bunch quality. In an IOA, the emitted electrons must pass the influence of the gate and enter the monotonic anode potential field in less than one-third of the period. For parallel plane electrodes δ_{gc} apart, the transit time is $\tau = \delta_{gc} \sqrt{2m_e / eV_{gc}}$, giving $V_{gc} / \delta_{gc}^2 \geq 2(m_e/e)(3f)^2$. For gridded thermionic cathodes in high-power applications, an optimistic estimate of $\delta_{gc} = 500 \mu\text{m}$, and $V_{gc} = 100 \text{ V}$ gives a maximum frequency near 2 GHz; for a typical FEA, δ_{gc} is on the order of $1 \mu\text{m}$, and the corresponding transit-time-limited frequency is 1 THz. Since V_{gc} must be held down to maintain the gain and efficiency of the amplifier, it follows that the grid-cathode assembly must be miniaturized for high frequency operation (i.e., if the dc grid bias potential is raised, the current ratio drops and efficiency is reduced; if the rf grid potential is increased to compensate, the gain is reduced.) Whether or not the current comes from field emission, the use of microfabricated structures is unavoidable above a few gigahertz.

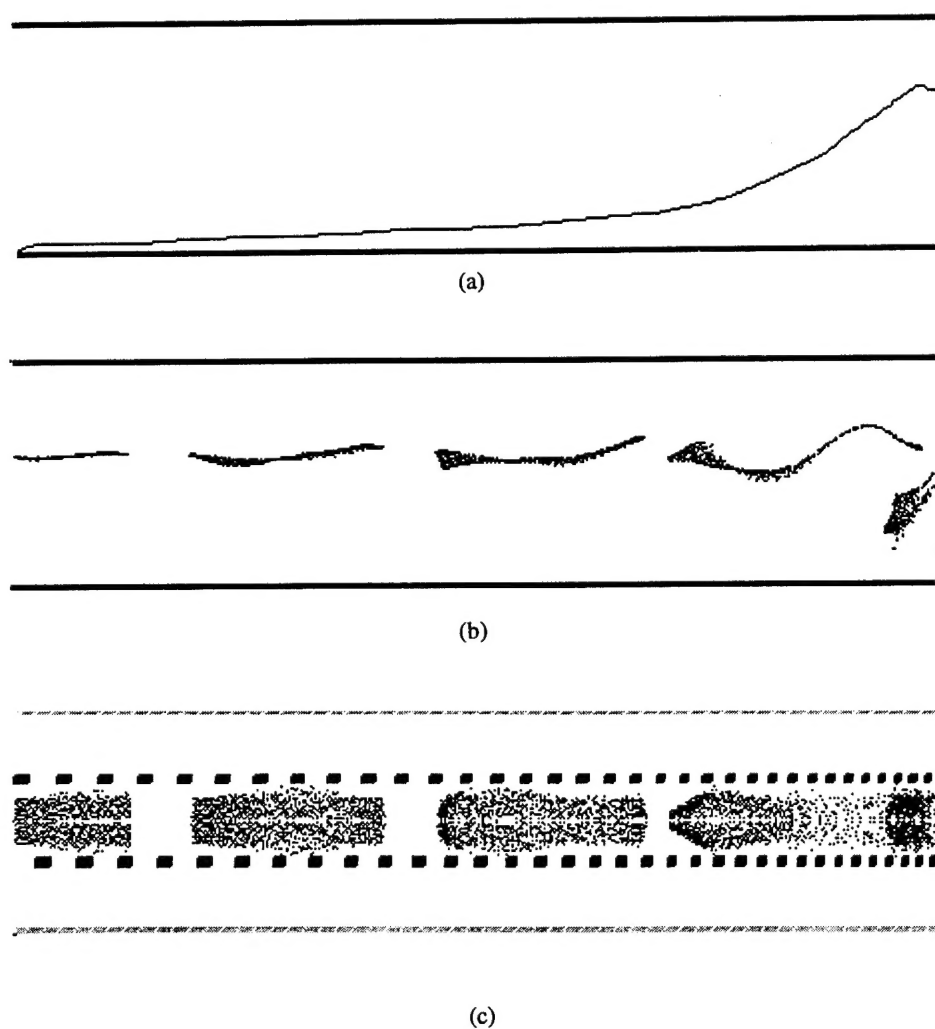


Fig. 3 — Phase space of electrons in a radically tapered helix: (a) efficiency vs distance; (b) axial momentum vs axial position; and (c) beam cross-section.

3.2. Transconductance

The transconductance g_m of a voltage-controlled current source is defined as the incremental change in beam current divided by the incremental change in gate potential: $g_m = \partial I_{beam} / \partial V_{gc}$. For the purpose of relating cathode performance to the gain of an IOA, a power transconductance g_p may be defined as the incremental current for an increment in drive power: $g_p = \partial i_b / \partial P_{dr}$, with units of amperes-per-watt. Usually emission-gating is performed by applying an oscillating potential to a gridded cathode, and the conversion becomes $g_p = g_m \partial V_{gc} / \partial P_{dr}$, where the relation between the drive power and the voltage at the gate depends upon the input circuit (to be discussed in the next section). For a photocathode, the power transconductance becomes

$$g_p = \frac{e \partial n_{electrons}}{\partial n_{photons}} \cdot \frac{1}{h\nu} \frac{\partial P_{laser}}{\partial P_{dr}} = \frac{e}{h\nu} \cdot \eta_{cathode} \cdot \eta_{rf \text{ laser modulation}}$$

The initial constant being of order unity, the efficiency of the photoemitter becomes the limiting factor in the use of photocathodes for vacuum amplifiers.

3.3. Capacitance

In a gridded cathode, the gate and the emitting surface form a capacitive load on the rf input circuit. Figure 4 shows the source represented by its Thevenin equivalent. The impedance transformation may take many forms—for example, quarter-wave lines, stub tuners, or tapered impedances. The FEA capacitance, its external resonant inductance, and the feed lines typically form a low-Q termination. The power required for a voltage swing V_{rf} on the gate is $P_c = \frac{1}{2} \omega C V_{rf}^2$, where V_{rf} is defined by $V_{gc} = V_{bias} + V_{rf} \sin \omega t$. In a resonant circuit, this is equal to the reactive power exchanged between the inductance and the capacitance: $P_{reac} = \frac{1}{2} \omega_0 C V_{rf}^2$. Additional power is required to overcome resistive losses in the circuit; at resonance this is equal to the available power supplied by the driver in each cycle. The ratio P_{reac} / P_{avail} is the quality factor Q of the resonant circuit, leading to $P_{avail} = \frac{1}{2Q} \omega_0 C V_{rf}^2$. If the impedance transformation is perfect and lossless, the required drive power is $P_{dr} = 2P_{avail}$, or $P_{dr} = \frac{1}{Q} \omega_0 C V_{rf}^2$. This result, valid at the resonant frequency, assumes that the characteristic impedance of the input transmission line can be matched to the load, while ignoring losses and reflections in impedance transformers outside the resonant loop. If the impedances cannot be matched (and a typical FEA has a real impedance on the order of 1Ω or less) then the required drive power will be increased by an additional factor of

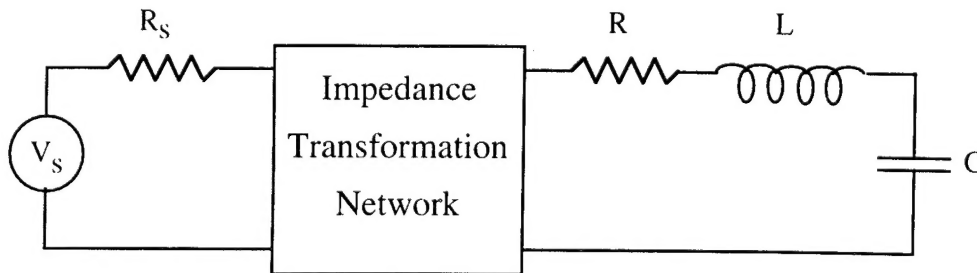


Fig. 4 — Series RLC circuit for rf input

$$P_{dr} = \frac{1}{4} \left(\sqrt{\frac{R}{Z_0}} + \sqrt{\frac{Z_0}{R}} \right)^2 P_{load},$$

which may cost 10 dB or more of gain. At off-resonant frequencies, the inductance will not supply all of the reactive power; the required drive power will increase as

$$\frac{P}{P_{res}} = \left[1 + Q^2 \left(\frac{\omega}{\omega_0} - \frac{\omega_0}{\omega} \right)^2 \right]^{\frac{1}{2}},$$

to maintain the same current in the resonant circuit and thus the same gate voltage amplitude V_{rf} . (Q is the quality factor of the resonant circuit.) Finally,

$$P_{dr} = \frac{\omega_0 C}{4Q} \left(\sqrt{\frac{R}{Z_0}} + \sqrt{\frac{Z_0}{R}} \right)^2 \left[1 + Q^2 \left(\frac{\omega}{\omega_0} - \frac{\omega_0}{\omega} \right)^2 \right]^{\frac{1}{2}} V_{rf}^2. \quad (1)$$

It is apparent that the performance of the cathode will dominate the gain of an inductive output amplifier: specifically there is a tradeoff between the Q (i.e., the fractional bandwidth), the gate-to-cathode capacitance, and the gain. For a 10 pF cathode with a 3% bandwidth at 10 GHz and requiring a 10 V gating signal (20 V p-p) the band-center drive power is 0.5 W. If the series-resonant RLC circuit with $R = 1 \Omega$ must be fed by a stripline with $Z_0 = 10 \Omega$ (about the minimum impedance for a low loss stripline), then the required drive power increases to 5.5 W.

3.4 Gain

From the above discussions of transconductance and capacitive loading, we derive

$$\begin{aligned} g_P &\equiv \frac{\partial i_b}{\partial P_{dr}} \\ &= g_m \frac{2Q}{\omega_0 C V_{rf}} \left(\sqrt{\frac{R}{Z_0}} + \sqrt{\frac{Z_0}{R}} \right)^{-2}. \end{aligned} \quad (2)$$

This useful figure of merit for the emission-gating assembly correlates closely to the gain of the complete amplifier. (It can be shown that the product $g_P \bullet P_{dr}$ is dependent only on the average and peak beam currents.) In this relation, the appearance of the transconductance, bandwidth, frequency, and capacitance are predictable and obvious, but the rf gate-to-cathode voltage is an odd fundamental design parameter. It is intuitive that an increase in the rf voltage will increase the depth of modulation of the electron beam; without assuming a specific form for the characteristic curve $I(V)$, we can linearize it to $g_m \approx \Delta I / \Delta V$, where ΔI and ΔV are identified with the rf components of the beam current and gate voltage. The power transconductance then takes the form

$$g_P \equiv \partial b / \partial P_d = \frac{2g_m^2}{R(\omega_0 C)^2 \Delta I} \left(\sqrt{\frac{R}{Z_0}} + \sqrt{\frac{Z_0}{R}} \right)^{-2}, \quad (3)$$

which makes the point that in emission-gating, there is a price in gain for a strongly modulated beam. We will show in Section 5 that this leads to a tradeoff between the gain and the efficiency (and/or the compactness) of inductive output amplifiers. In Section 4, this figure of merit will be related to the geometry and materials of FEA cathodes.

3.5. Current Density

Since gain is inversely proportional to the gate-to-cathode capacitance, a small-area source operating near peak intensity will generally provide the best simultaneous gain and efficiency. This raises issues in electron gun design, including initial velocity effects, beam spreading, axial demodulation, beam stability, and perveance enhancement. All are of concern in a design context. Here we are particularly interested in any enhancement in gun perveance that would enable use of the extremely high current densities available from field emission sources, perveance being the constraint on the maximum current which can be drawn for any specified anode voltage, $I = KV^{3/2}$.

The conventional starting point in predicting the gun perveance K is the one-dimensional Child's law, or $J = (2.33 \cdot 10^{-6} / d^2) V^{3/2}$, where d (meters) is the anode-cathode gap distance. If the dimensions associated with the emitting area A are large compared with d , then the maximum current that can be drawn can be obtained by substituting the Child's law result into $I = JA$. Thus, for example, a solid beam diode with $A = \pi r^2$, $r > d$ has a perveance that is well approximated by $K = (2.33 \cdot 10^{-6} / d^2) \pi r^2$. However, annular beams are likely to be subject to the condition, $d \gg w$. To investigate this regime, MAGIC simulations were performed using a parallel-plate geometry in Cartesian coordinates (Fig. 5). Table 1 gives the simulation parameters and their ranges of variation. The procedure for each simulation was the same: the current density supplied at the cathode was gradually raised while observing electric fields everywhere in the gap. The simulation was terminated when field inversion occurred (invariably at the cathode surface), and peak current was then recorded as a function of the parameters. Surprisingly, the beam initial energy and the magnetic field had very little effect on the results. There was little spreading due to space charge, with maximum transverse energies typically of the order of a few electron volts—similar to the energy that would be imparted by the FEA gate. This transverse component typically appeared very near the cathode surface, where the velocity was lowest and the density highest. By inspection, we concluded that space-charge repulsion would cause almost no degradation of the bunching of a thin beam.

Modeling the annular beam diode in light of the calculated results, we find the gun perveance to be well represented by the fitting function

$$K = (2.33 \cdot 10^{-6} / d^2) 2\pi r w (1 + 2d/w)^{1/2}, \quad (4)$$

where the enhancement factor $(1 + 2d/w)^{1/2}$ is seen to be substantial for $d \gg w$. (The enhancement results from spreading of the image charge over the cathode; in a truly one-dimensional problem, the image charge is restricted to the emitting area.) Obviously, the idealized result of Eq. (4) must be modified to account for geometrical complexities such as a hollow anode, beam compression, etc. But our conclusion is that, for annular beam diodes, it is possible to draw a large multiple of the current calculated from the 1-D Child's law and the emitting area.

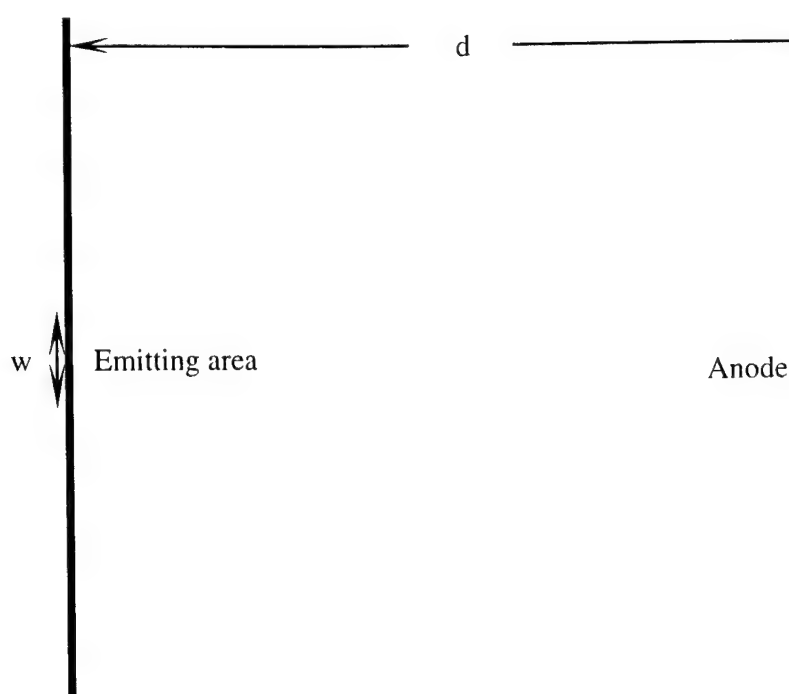


Fig. 5 — Sheet beam diode simulation geometry

Table 1 — Hollow Diode Simulation Parameters

V (AK voltage)	1.0 - 10.0 kV
d (AK gap)	0.2 - 2.0 mm
d/w (gap-to-width)	0.75 - 30
B (magnetic field)	0.2 - 4.0 T
T (initial energy)	1.0 - 10.0 eV

Because such high-perveance beams improve the performance of rf output couplers, it is advantageous to draw the maximum current density consistent with a reasonable cathode lifetime. Figure 6 compares the perveances and the required current densities of two planar diodes—a solid beam of outer radius r and anode separation d and a hollow beam of the same outer radius and separation with annulus width w . The solid line gives the annulus width for which the annular diode has the same perveance as the solid diode, while the dotted lines give the ratio of the beam current density required to obtain the same total current from the hollow diode. The figure shows that practical annular designs can take advantage of emission current densities an order of magnitude larger than a 1-D planar diode. Electron guns for inductive output amplifiers should be designed to exploit cathodes, such as FEAs, which are capable of emitting hundreds of amperes per square centimeter.

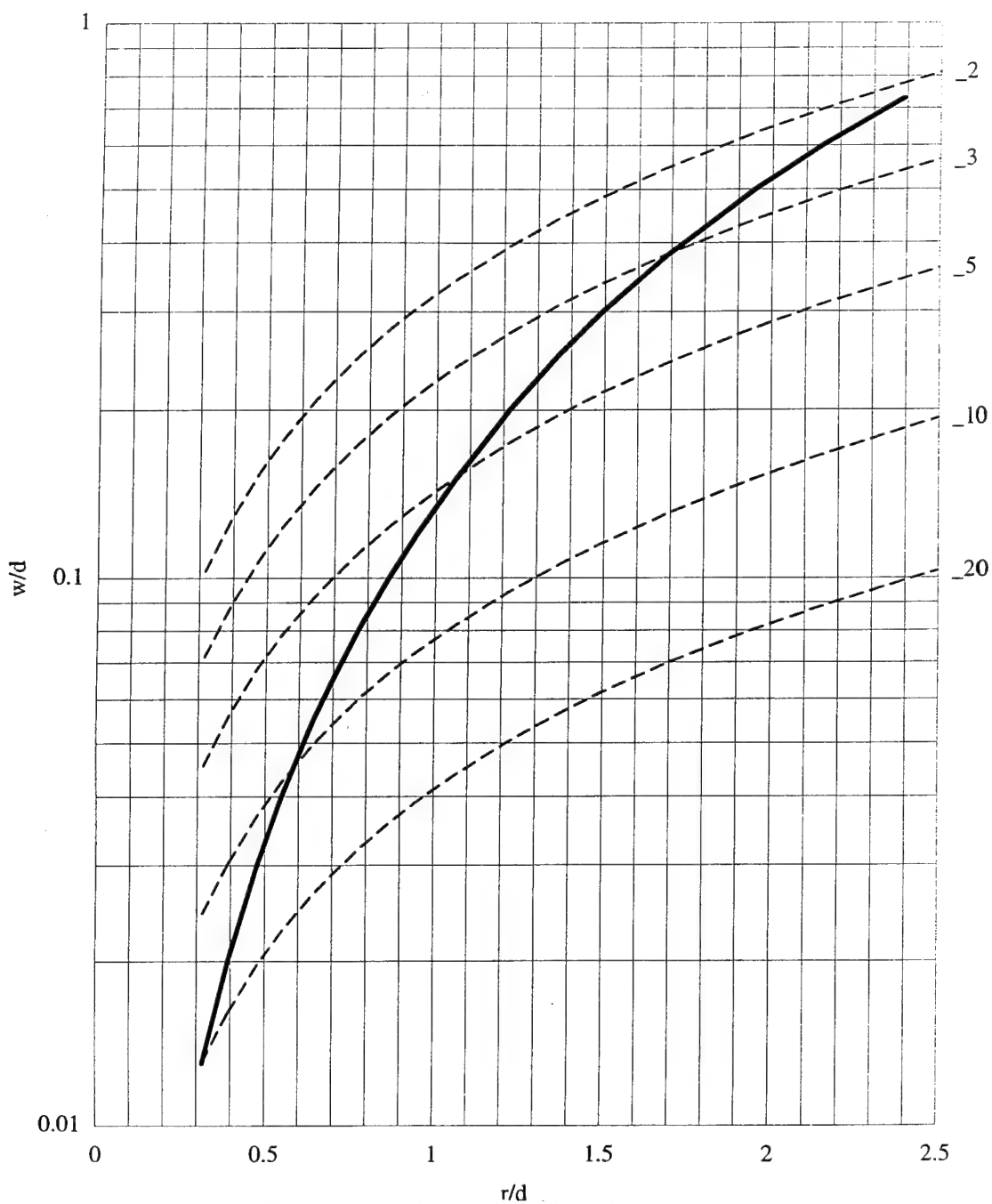


Fig. 6 — Perveance and current density ratios of solid and hollow beams

4. CATHODE OF CHOICE—FEAs

Field emission arrays have long been recognized as promising replacements for thermionic emitters in vacuum microwave amplifiers due to their instant turn-on and high current density capabilities. The vertical-emitter gated FEA structure consists of a conducting "base" plane supporting sharply pointed "tips" of cones or ridges and an electrically isolated conducting "gate" plane with apertures through which electrons pass out of the structure. Figure 7 is a diagram of an FEA unit cell. A predictive model for the current-voltage characteristic of novel FEA structures is needed to reduce the time and cost of trial-and-error development. Such a model, combining analytical and computational elements for maximum accuracy and utility, has been constructed.[17] We present a summary of the physics and structure of the model below, concentrating upon the implications for the cathode figure of merit g_p given by Eq. (2).

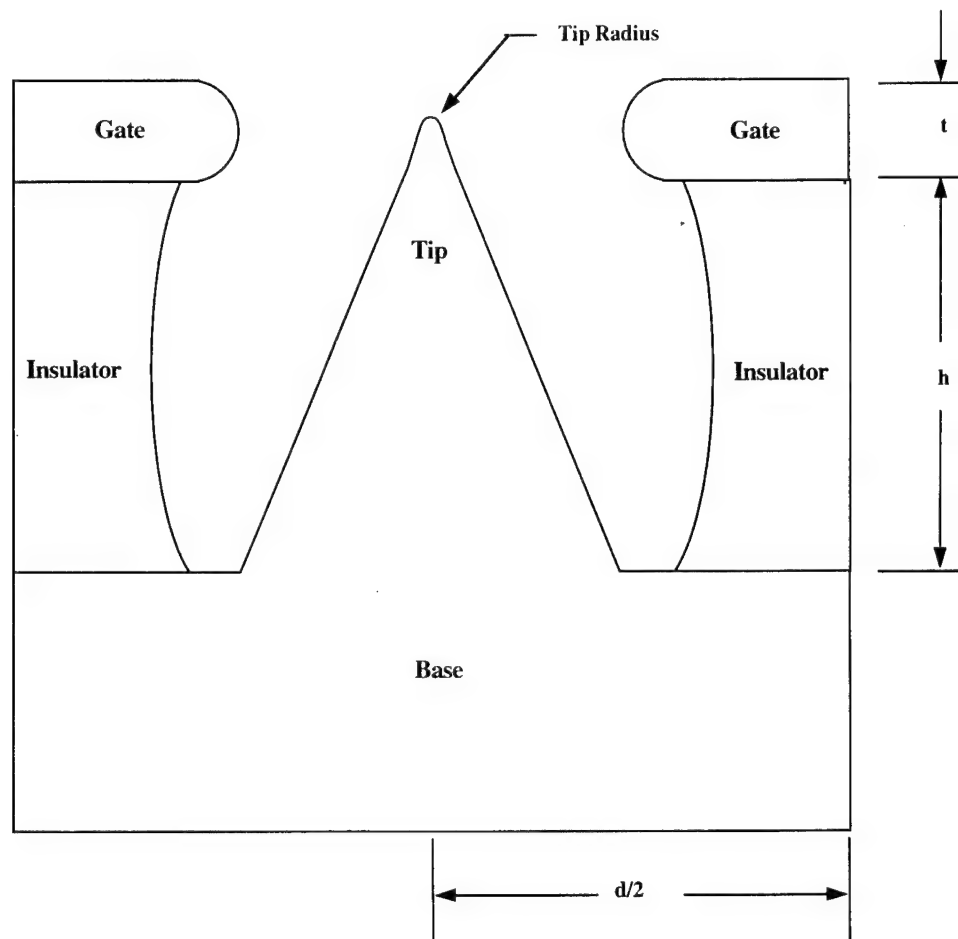


Fig. 7 — An FEA unit cell

4.1 Current vs Gate Voltage Modeling

A widely used method of estimating the field emission current density J from a tip is to approximate the applied field dependence of J by the 1-D Fowler-Nordheim $J_{FN}(F)$, which depends upon the local applied field F :

$$J_{FN}(F) = a_{FN} F^2 \exp\left(-\frac{b_{FN}}{F}\right), \quad (5)$$

where a_{FN} and b_{FN} are material-dependent. [18,19,20] The total current from an arbitrarily shaped emitter is then given by integration over the surface

$$I(V_g) = \int_S \vec{J} \cdot d\vec{S}. \quad (6)$$

The Fowler-Nordheim relation is often applied to field emission from three-dimensional structures by making the simple replacements $I = b_A J$ and $F = \beta V_g$ (a procedure that has been roundly criticized [21,22] but nevertheless widely used) in order to "derive" current-voltage relations amenable to fitting experimental current-voltage data:

$$\begin{aligned} I(V_{gc}) &= b_A a_{FN} \beta^2 V_{gc}^2 \exp(-b_{FN}/\beta V_{gc}) \\ &\equiv A_{FN} V_{gc}^2 \exp(-B_{FN}/V_{gc}). \end{aligned} \quad (7)$$

The (assumed constant) parameters A_{FN} and B_{FN} are strictly empirical due to the *ad hoc* nature of the "area factor" b_A and "field enhancement factor" β . The problem of "measuring" J and F has simply been deferred to "measuring" b_A and β .

The simplest model of a gated field emitter is obtained by replacing the field emitter tip by a sphere, the gate by a ring, and the influence of the anode by a constant background field (Fig. 8). The resulting "Saturn" model [23] provides analytically tractable relations between the total current emitted from the sphere, the tip and gate radii, and the potential of the gate. The methodology is similar to that employed for the emitters in a diode configuration.[24] Taking the origin of coordinates to be the center of the sphere, the angular dependence of the field in the vicinity of the tip apex (i.e., for $r = a_s$ and θ small) may be approximated by:

$$F(\theta) = \frac{F_{tip}}{1 + \lambda(1 - \cos \theta)}, \quad (8)$$

where F_{tip} is the field on-axis. The Saturn geometry accurately models the tip and the anode field; however the ring model of the gate breaks down at high gate potentials as all the space charge is concentrated close to the tip. The model may be improved by the adding rings of successively larger radius, to better approximate a hole in a gate plane. These rings modify the parameters F_{tip} and λ , providing more quantitatively correct results without modifying the form of the solution. This, however, begins to look like a fully discretized model such as that described next.

The boundary element method replaces the surfaces inherent in Eq. (6) with ribbons having a (constant) surface charge density (Fig. 9), where attention is restricted to cases with azimuthal symmetry.[25,26,27] The azimuthally symmetric structure is divided into ribbons; accuracy is enhanced by dramatically reducing the widths of ribbons near the tip. Equation (5) then becomes a matrix equation of the form $\phi = \mathbf{M} \cdot \sigma$. As the potential distribution ϕ is known, the equation can be inverted to find the surface charge vector σ . The field on each charged ribbon is proportional to the surface charge of that ribbon and so the total current from the tip may be found by summing over the current from each ribbon. Further, as the total charge on the tip is known, the tip-gate capacitance can be found (as well as other components of the capacitance matrix). Though the method is relatively fast (the sequence of programs takes less than a minute to generate an $I(V_g)$ curve), the influence of geometry and materials on the emitted current is not transparent.

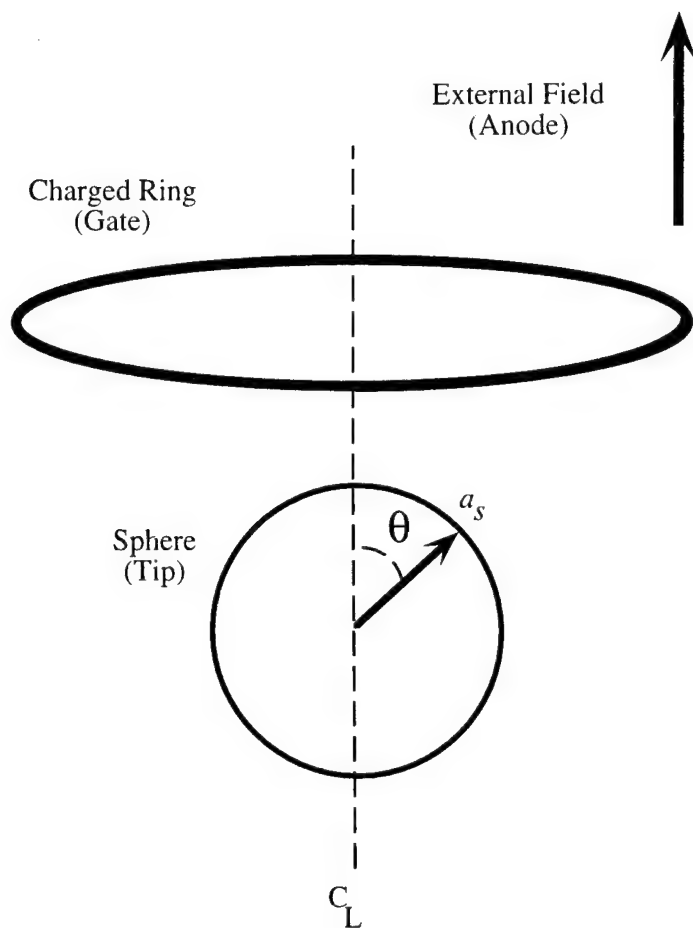


Fig. 8 — The Saturn model, with a spherical tip and ring gate

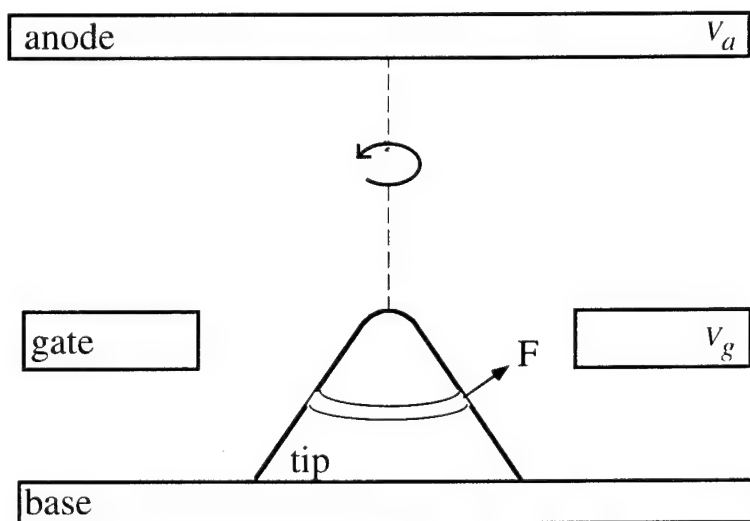


Fig. 9 — The boundary element model

A hybrid of the two aforementioned approaches, the "semi-numerical" model, substitutes accurate values of the critical parameters F_{tip} and λ from the boundary element model into the intuitively appealing Saturn model. The semi-numerical model therefore combines the best features of both and has further been shown to successfully match experimental $I(V_g)$ characteristics. The semi-numerical model assumes the form of Eq.(8), but further lets F_{tip} and λ be functions of the gate voltage:

$$F_{\text{tip}}(V_g) = \beta_f V_g + Y_f, \quad (9)$$

$$\lambda(V_g) = (\beta_\lambda / V_g) + Y_\lambda, \quad (10)$$

where β is the slope, in keeping with the conventional use of β for the field enhancement factor. Due to the linearity of Eqs (9) and (10) in V_g and its inverse, any two boundary element solutions at different gate potentials determine the β and Y parameters for a given geometry. Similar arguments apply to capacitance, as we have from the capacitance matrix:

$$C(V_g) = C_{tg} + C_{ta} V_a / V_g, \quad (11)$$

where the a subscript refers to the anode and the tip-to-gate capacitance C_{tg} is therefore the y-intercept of $C(V_{gc})$. The Fowler Nordheim parameters A_{FN} and B_{fFN} are obtained from a linear fit of $\ln[I/V_g^2]$ vs $1/V_g$ in the V_g range of interest. The substitution of accurate parameters from the boundary element calculation into the Saturn model's analytical relationships gives an excellent model of FEA performance.

Simulations were performed to establish the dependence of A_{FN} and B_{FN} upon tip radius a_s and gate radius r_g for fixed relationships with other geometrical parameters. In one example, a sphere on cone triode geometry is described: the work function is 4.35 eV, the tip-to-tip distance is $10 \cdot r_g$, the base to the gate midplane equal to the tip height above the base, both at $2 \cdot r_g$, the gate thickness at $0.5 \cdot r_g$, the 200-V anode $10 \mu\text{m}$ above the gate. The tip radius was varied from 5 \AA to 100 \AA , and the gate radius was varied from $0.02 \mu\text{m}$ to $0.5 \mu\text{m}$. The Fowler-Nordheim A_{fn} per tip varies linearly for $a_s/r_g > 100$ with the form:

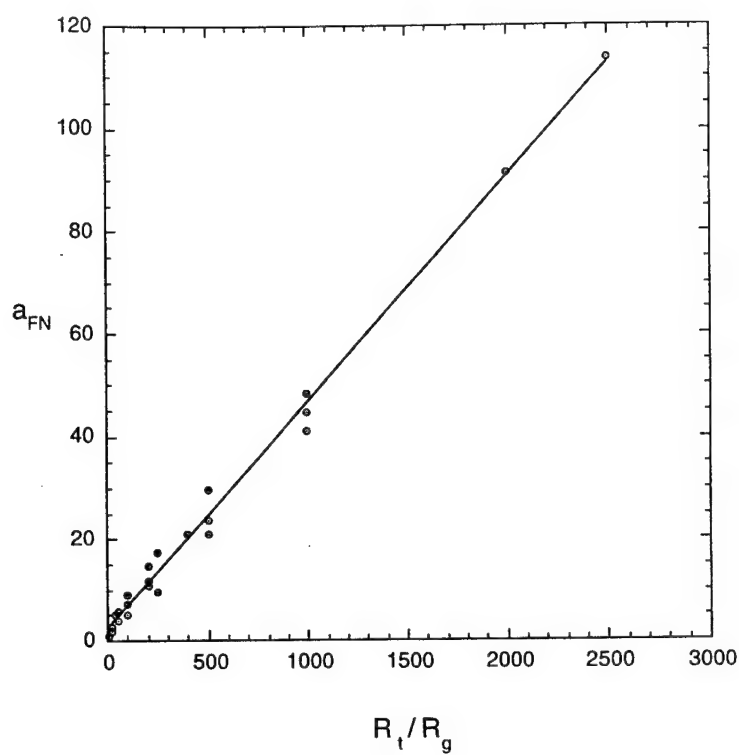
$$A_{FN} \left[\frac{\mu\text{A}}{\text{V}^2} \right] = 2.53 + 441 \cdot \frac{a_s}{r_g}, \quad (12)$$

as shown in Fig. 10(a) The Fowler-Nordheim B_{FN} varies logarithmically in the gate radius with the form:

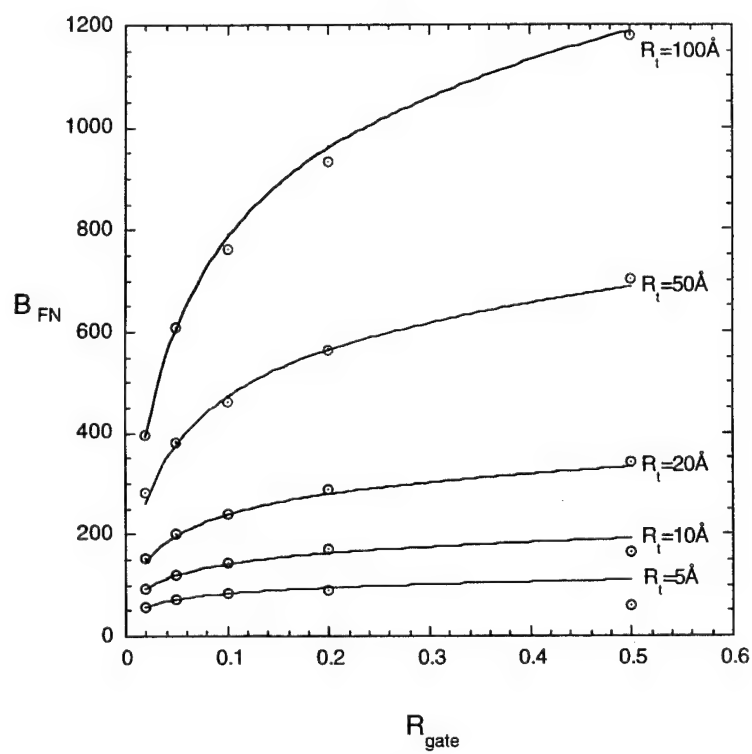
$$B_{FN}[\text{V}] = \left\{ 33.4 a_s^{0.8} + 8.75 a_s^{0.9} \cdot \log(r_g) \right\} \quad a_s \text{ in } [\text{\AA}], r_g \text{ in } [\mu\text{m}], \quad (13)$$

as shown in Fig. 10(b). For small gate radius, the B_{FN} becomes attractively small, but its extreme sensitivity to the gate radius may present a new uniformity problem. The gate-to-tip capacitance per tip (which excludes the gate-to-base capacitance) is given by:

$$C_{tg}[\text{pF}] = 3.7 \cdot 10^{-7} + 4.7 \cdot 10^{-5} \cdot r_g[\mu\text{m}]. \quad (14)$$



(a)



(b)

Fig. 10 — Parametric fit of (a) A_{FN} and (b) B_{FN}

The increase of capacitance with gate radius is counterintuitive. However, the base-to-gate distance and gate thickness are also scaled with gate radius in this example and is the source of this additional capacitance.

4.2 Gated FEA Figure of Merit

The power transconductance of a modulated cathode, defined in Eq. (2), may now be calculated for the specific case of gated field emission. Substituting the conventional transconductance g_m , the derivative of Eq. (7), and the derivative of Eq. (1), we obtain

$$g_P = N_{tips} A_{FN} (2V_{pk} + B_{FN}) \exp\left(-\frac{B_{FN}}{V_{pk}}\right) \cdot \frac{2Q}{V_{rf} \omega_0 C_{total}} \left(\sqrt{\frac{R}{Z_0}} + \sqrt{\frac{Z_0}{R}}\right)^{-2}, \quad (15)$$

where evaluation at the maximum value $V_{pk} = V_{bias} + V_{rf}$ is an appropriate choice for strongly modulated beams. (Evaluation at the center frequency is also assumed.) The total number of emitting tips is N_{tips} , and the total capacitance is given by: $C_{total} = C_{add} + N_{tips} C_{tip}$, where C_{tip} is the total capacitance for each unit cell, and C_{add} is any effective capacitive load in addition to the sum over the FEA unit cells. Defining $i_{pk} = A_{FN} V_{pk}^2 \exp(-B_{FN}/V_{pk})$, the peak current per tip, and noting that $N_{tips} i_{pk}$ is the peak beam current I_{pk} we obtain:

$$g_P = \frac{I_{avg}}{\left(I_{avg}/I_{pk}\right)} \frac{2V_{pk} + B_{FN}}{V_{pk}^2} \cdot \frac{2Q}{V_{rf} \omega_0 (C_{add} + N_{tips} C_{tip})} \left(\sqrt{\frac{R}{Z_0}} + \sqrt{\frac{Z_0}{R}}\right)^{-2}. \quad (16)$$

The rf voltage V_{rf} can be obtained in terms of the modulation current ratio I_{avg}/I_{pk} by convolution of the gate voltage signal upon Eq. (7). For $I_{avg}/I_{pk} < 0.4$, the result is:

$$V_{rf} = \frac{1}{2\pi \left(I_{avg}/I_{pk}\right)^2} \frac{V_{pk}^2}{2V_{pk} + B_{FN}}, \quad (17)$$

yielding finally:

$$g_P = \frac{4\pi Q A_{FN} \exp(-B_{FN}/V_{pk})}{\omega_0 \left(\frac{C_{add}}{N_{tips}} + C_{tip}\right)} \left(I_{avg}/I_{pk}\right)^2 \left(2 + \frac{B_{FN}}{V_{pk}}\right)^2 \left(\sqrt{\frac{R}{Z_0}} + \sqrt{\frac{Z_0}{R}}\right)^{-2}. \quad (18)$$

The effects of the input circuit bandwidth and the mismatch are obvious, and the modulation current ratio should be kept as large as is consistent with acceptable efficiency (Section 5).

More interestingly, this relation offers several hints for the optimization of FEAs for maximum gain. The $I(V)$ characteristic curve and the capacitance are the FEA characteristics that appear here; in other words, the FEA is effectively described by A_{FN} , B_{FN} , and C with the operating point given

either by i_{pk} or V_{pk} . The gain is most sensitive to the exponential implicit in Eq. (7), and reducing B_{FN} is the most effective means of optimizing the FEA. The two parameters A_{FN} and C occur only as the ratio A_{FN}/C ; they may be traded-off against each other.

5. EFFICIENCY

The output circuit has relatively little effect on the gain of IOAs but will largely determine the efficiency and the compactness of the device. Any output geometry that is employed with velocity-modulated beams may be used to couple power from an emission-gated beam, though an optimized IOA output circuit will have different specifications than a corresponding velocity-modulated output section. We will discuss this optimization for two circuits representing extremes of bandwidth and compactness: a pi-mode klystron cavity and a helical twystron circuit.

Here we present the performance criteria for output circuits in inductive output amplifiers. The design constraints which force tradeoffs will then be reviewed for representative klystron and twystron circuits. The klystron circuit is a pi-mode cavity chosen for its useful combination of bandwidth and interaction efficiency; for the wideband twystron, a helical circuit offers excellent bandwidth with ease of velocity-tapering to maximize efficiency as well. In Section 6, we illustrate the tradeoffs between gain and efficiency with several examples chosen to highlight the requirements for emission-gated electron sources.

5.1. Performance Criteria

The output circuit is the major determinant of the efficiency and specific power of the amplifier. Specific power is the ratio of output power to volume (or weight for some applications), and the output circuit is typically the largest of all components of the amplifier. Efficiency is defined as the usable output power divided by the input beam power. In general, it will depend strongly on the current ratio I_a/I_p . If the bunch shape derives from the macroscopic Fowler-Nordheim current characteristic (Eq. 7), then the current ratio becomes

$$\frac{I_a}{I_p} = \frac{\frac{\omega}{2\pi} \int dt A (V_{bias} + V_{rf} \sin \omega t)^2 e^{-B/(V_{bias} + V_{rf} \sin \omega t)}}{A (V_{bias} + V_{rf})^2 e^{-B/(V_{bias} + V_{rf})}}. \quad (19)$$

Intuitively, one might expect that a strongly modulated beam (lower I_a/I_p) would result in superior efficiency. However, in a broadband output circuit (twystron), a strongly modulated beam drives higher frequency parasitic modes that can reduce efficiency. In narrowband output circuits (klystrons), the high frequency modes on a strongly modulated beam pass through the circuit without exciting parasitic modes but contribute significantly to the peak electric field in the gap, which limits the power handling capability of the output cavity. In both circuits, strong modulation severely reduces the gain (Section 3.4), and this mitigates against simply maximizing efficiency.

5.2. Klystron

Output circuit efficiency for the klystron can be predicted using techniques ranging from basic analytical theory to detailed electromagnetic particle-in-cell (PIC) simulation. Resonator saturation theory (RST) [28] is an analytical approach that predicts the power in the output cavity from startup through saturation. It is based upon conservation of energy expressed by:

$$\frac{dW}{dt} = -\frac{\omega_0}{Q} W + \langle E \cdot J \rangle,$$

where W is the cavity energy and $\langle EJ \rangle$ is the power loss of the beam. The power loss term is calculated by integrating the electron velocities crossing the gap with sinusoidally varying voltage. For integrable bunch shapes and small transit angles, a complete analytical result is obtained. When analytic criteria are not met, the power loss term can be integrated numerically, including details such as arbitrary bunch and interaction field shape, etc. Thus, resonator saturation theory is the basis for the KLYDE code [31]. The code optimizes the peak circuit voltage and the beam-to-circuit phase shift for maximum beam power loss (efficiency), subject to constraints on the peak electric field and the prohibition of electron backstreaming.

When space charge is important, one can resort to multidimensional, electromagnetic PIC techniques such as MAGIC [29] to obtain a fully self-consistent check on KLYDE. In the PIC code, the circuit can be modeled with a full-cavity transient simulation or with a "port approximation" similar to that used in KLYDE. The predictive accuracy of these methods has been well substantiated, most notably for the 487 MHz klystrode design by Varian.[12]

To illustrate the effect of the current ratio upon klystrode performance, we have calculated the maximum efficiency that can be obtained from a pi-mode cavity circuit with the specifications given in Table 2. Figure 11 illustrates the geometry for an idealized pi-mode cavity. In the simulations, the two gap widths were assumed to be the same, so that the gap fields were equal in magnitude but opposite in sign. Then the gap width d_g and spacing d_s were systematically varied along with the gap voltage and bunch phase to maximize efficiency, subject to mechanical (spacer size $> *$), peak field ($E_z < 100$ kV/cm) and electron reversal ($P_z > 0$) constraints. This optimization procedure was repeated for current ratios in the range $0.2 < I_a/I_p < 0.8$, and the results were then fit to the following expressions for optimum efficiency and quality factor:

$$\begin{aligned} \eta_{opt} &= (1 - I_a/I_p) (1 - I_a/3I_p) \\ Q_{opt} &= 300 (I_a/I_p) \left\{ 1 + 2 (I_a/I_p)^4 \right\}. \end{aligned} \quad (22)$$

Subject to the constraints, η_{opt} represents the highest efficiency that could be obtained at that current ratio by redesigning the cavity for that ratio. The optimum quality factor Q_{opt} is the cavity Q required to achieve the maximum efficiency at that current ratio. Although efficiency clearly increases as current ratio decreases, low current ratios may result in unacceptably poor gain. This tradeoff is seen in the examples of Section 6. That the Q varies with the current ratio, thus inversely to the efficiency, is the usual behavior of cavity circuits. For wider bandwidth with acceptable efficiency, one would abandon the simple pi-mode structure for a coupled-cavity circuit.

5.3. Twystrode

A twystrode is an inductive output amplifier with a synchronous traveling-wave output circuit. For the present analysis, we have selected a helical circuit, modeled as a sheath helix with moderate vane and shell loading for moderate dispersion, resembling the output section of a traveling-wave tube. However, in contrast to the TWT for which linear Pierce theory [30] is good to first order, the interaction of a prebunched beam and a helix is nonlinear. The mode amplitudes of both the electromagnetic and space charge waves vary orders of magnitude per wavelength, leaving no slowly varying or adiabatic variable upon which to base a linearization. With the recent development of the polarizer model, detailed simulation of the complete output circuit is now practical.

Table 2 — Klystrode Simulation Parameters

$f = 10 \text{ GHz}$
$I_a = 60 \text{ mA}$
$V_b = 2.5 \text{ kV}$
$R_b = 0.3 \text{ mm}$
$R_t = 0.45 \text{ mm}$
$B = 0.4 \text{ Tesla}$

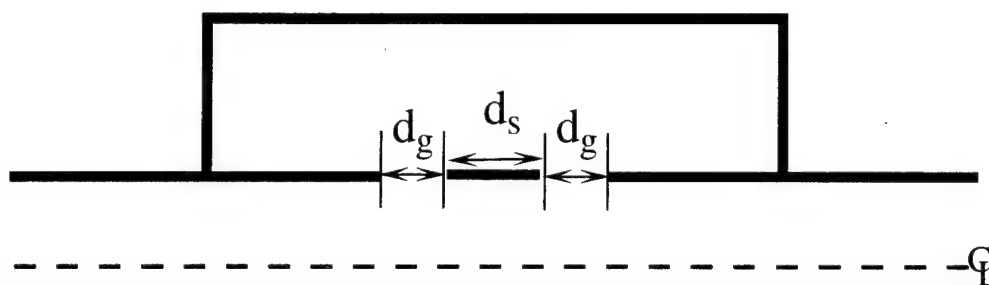


Fig. 11 — The pi-mode cavity

The polarizer model [31] uses a sheath approximation in which the finite-wire helix is represented as a cylindrical sheet with infinite conductance parallel to the helix wire and zero conductance in the perpendicular direction. This representation, realized as a boundary condition on the fields, enables accurate modeling of a helical circuit in a 2-D particle-in-cell simulation. The model is implemented in MAGIC as a projection operator that constrains axial and azimuthal fields at the helix radius. Special diagnostics have been developed to analyze fundamental mode power as a function of axial distance. This model has been in use for several years and is in excellent agreement with the series of emission gated amplifier experiments [13, 14, 32]

Exercise of the model over a broad range of parameter space indicated that efficiencies much exceeding 20% were unobtainable with a constant-pitch helix. Upon introduction of a quadratically tapered pitch and a 3-stage collector post-processor, the best net efficiencies appeared at unexpectedly large taper ratios, e.g., 3:1. Work then focused on optimizing such radically tapered helices by adjusting the parameters a_n in the pitch equation $P(z) = 2\pi R_h \tan(a_0 + a_1 z + a_2 z^2)$ to (1) minimize the accelerated "runaway" electron population and (2) to keep the decelerated electrons in a tight, nearly monoenergetic packet. This second constraint improved both single-pass and net efficiency by deferring reversal of the slowest electrons to lower net beam energies and by maximizing the collector efficiency.

To illustrate the effect of the current ratio upon twystrode performance, we have calculated the maximum single-pass efficiency for a radically tapered design, with the parameters given in Table 3. The efficiency was optimized with respect to the quadratic pitch equation, including the total length

of the circuit, subject to the constraint of electron reversal. The results from this optimization exercise were then fitted to portray optimum single-pass efficiency and associated circuit length as a function of current ratio,

$$\begin{aligned}\eta_{opt} &= \left(\frac{1}{2} + I_a/I_p\right) \left(1 - I_a/I_p\right)^2 \\ L_{opt} &= 0.05 \left(I_a/I_p\right)^2.\end{aligned}\tag{23}$$

Table 3 — Twystrode Simulation Parameters

$f = 10 \text{ GHz}$
$I_a = 200 \text{ mA}$
$V_b = 4 \text{ kV}$
$R_b = 0.3 \text{ mm}$
$R_h = 0.45 \text{ mm}$
$R_t = 0.95 \text{ mm}$
$B = 0.75 \text{ Tesla}$

An experiment at 487 MHz and 3:1 tapered pitch is presently under way, and an FEA-driven experiment at 10 GHz is being designed. The specific results and recommendations of the model will continue to evolve; however, parabolic tapering and large variations in pitch appear most promising. Effective designs prevent runaway electrons, avoid reacceleration of slowed electrons, and maintain minimum velocity dispersion in the bulk of the electron bunch. In addition, we have evaluated the spent-beam $I(V)$ curves from numerous tapered helix designs and find that a three-stage, depressed collector would typically add 20 percentage points of efficiency over a broad range of current ratios. Thus, net efficiencies in excess of 50% appear likely for this device.

5.4. Further Development Under Way

For practical design, we must know how to extrapolate such results to nonoptimum quality factors and other regimes of frequency, beam power, voltage, average current, etc., and to connect circuit performance directly to FEA parameters. Many of these relationships are counterintuitive—for example, mechanical constraints on the pi-mode gap prevent scaling of length with frequency and, instead, lead to higher voltages. A complete description of the analysis methodology is beyond the scope of the present paper and will be reported separately [33].

6. EXAMPLES

A central question in the present state of the development of IOA with gated FEA cathodes is, "What FEA performance is required to meet realistic amplifier specifications?" The analysis presented in this paper can be used to make practical judgements on the feasibility of given designs or to state quantitatively the improvements required to make the designs feasible. To illustrate how this is done and to provide guidelines on minimum and optimal requirements, we will evaluate three FEA cathodes in both klystrode and twystrode amplifiers.

The three FEAs described in Table 4 also represent a range of performance from minimal to highly desirable. Note that FEA #1 is intended to be pie-in-the-sky— the best measurements to date. FEA #2 is intended to represent the current state of the art, which a designer could reasonably expect to obtain in quantity and with some reproducibility. FEA #3 is intended to demonstrate the necessity of low BFN for reasonable amplifier gain. The amplifier specifications are given in Table 5. Note that the frequency f_0 , the beam voltage V_{beam} , and the output power P_{out} , are nominally equal for all three amplifiers.

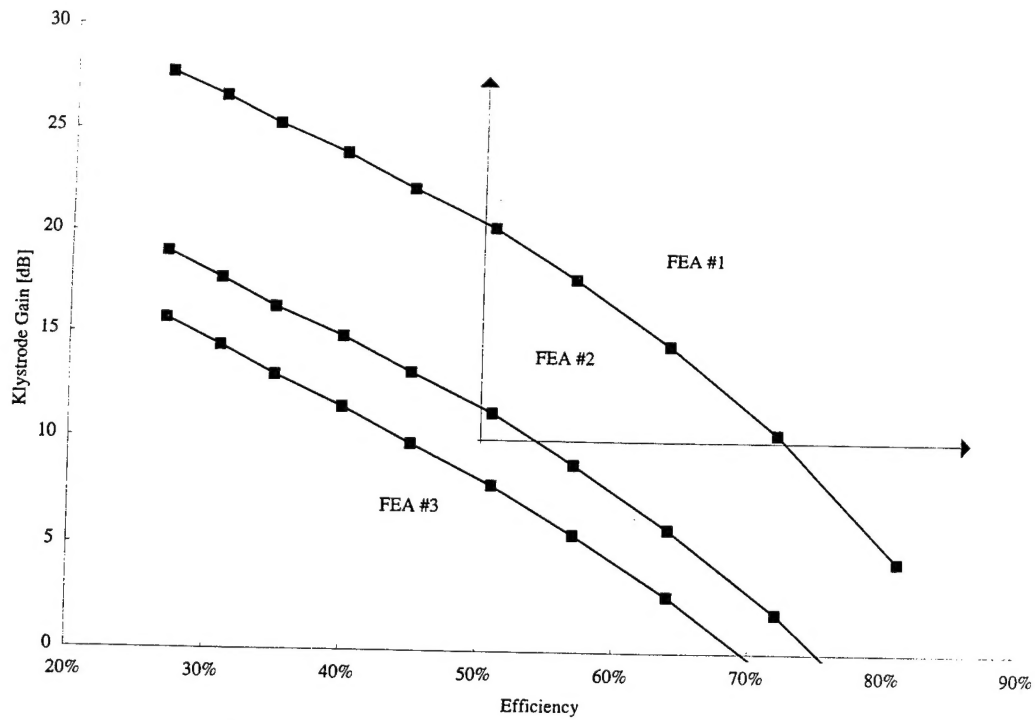
Table 4 — Amplifier Specifications

	FEA #1	FEA #2	FEA #3
a	$6.0 \mu\text{A}/\text{V}^2\text{tip}$	$8.5 \mu\text{A}/\text{V}^2\text{tip}$	$17.0 \mu\text{A}/\text{V}^2\text{tip}$
B	125 V	880 V	2000 V
C	5 pF total	10 pF total	2.5 pF total
i_{pk}	$1 \mu\text{A}/\text{tip}$	$10 \mu\text{A}/\text{tip}$	$20 \mu\text{A}/\text{tip}$
R	1.4Ω	1.4Ω	1.4Ω

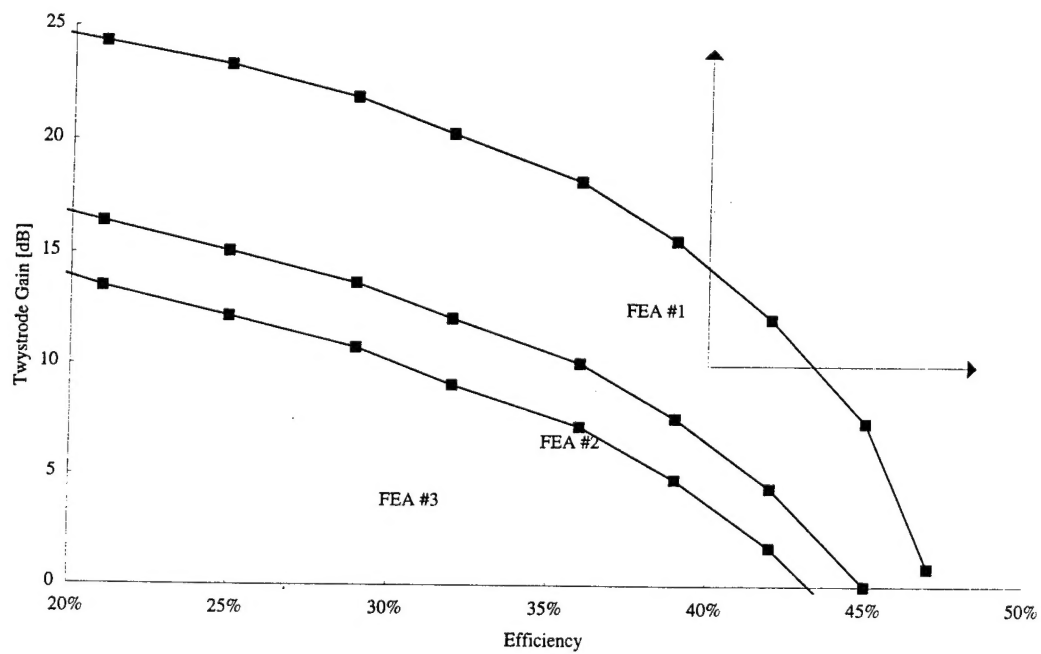
Table 5 — Three Examples of FEA Specifications

	Amplifier A	Amplifier B
f_0	10 GHz	10 GHz
BW	3%	33%
V_{beam}	2.5 kV	2.5 kV
P_{out}	50 W	50 W
Gain	10 dB	10 dB
Efficiency	50% net	40% net

Figures 12(a) and 12(b) show the gain and efficiency trade off of each amplifier; the arrows indicate the region on each plot where the specifications are met. Most noteworthy, FEA #1, representing a compilation of the best measured parameters available, does satisfy the specifications. The failure of FEA #3, due exclusively to large BFN because every other parameter is excellent, is a typical result of the analysis. Testing more than 100 possible combinations of FEA specifications by spreadsheet yielded uninteresting performance from any design with $BFN > 1000$, and no high-performing combination had $BFN > 500$. It is not surprising that there is no substitute for a small BFN ; equally unsurprising, reference to Eq. (13) indicates that small BFN comes from sharp tips and small gate apertures. At a BFN of 125 (and tip radius estimated under 10 \AA), FEA #1 is located in a region of Fig. 10(b) where order-of-magnitude improvement in performance may be expected for relatively slight reductions in size.



(a)



(b)

Fig. 12 — Gain vs efficiency: (a) klystrode; (b) twystrode

7. CONCLUSIONS

An Inductive Output Amplifier requires an emission-gated electron beam, obtained from a modulated source. Experiments and simulations have shown the advantages in compactness and efficiency obtainable by use of these prebunched beams. Simulations of a pi-mode cavity yielded 50% efficiency with acceptable gain and up to 3% bandwidth—further improvement in bandwidth would be obtained from a coupled-cavity output circuit. We find that while output circuits yielding net efficiencies of 50% or greater are well within the state of the art, the gain is likely to be moderate (10 to 20 dB). Design criteria for the joint optimization of the FEA structure and the RF input and output circuits of Inductive Output Amplifiers have been demonstrated.

Field emission cathodes, due to their extremely low electron transit time and high transconductance, offer the opportunity to extend the advantages of emission gating into C and X bands. With today's FEA performance, a desirable operating regime is achievable, yielding a new class of compact, highly efficient, and moderate gain power booster amplifiers.

ACKNOWLEDGEMENTS

The authors thank Drs. C. O. Bozler, R. A. Murphy, Rick Mathews, and Mark Hollis of MIT Lincoln Labs for making their experimental data ($I(V_g)$ and device geometry) available to us for comparison with theory and for many helpful discussions. Drs. Cap Spindt, Purobi Phillips, and Jonathan Shaw provided valuable clarification of FEA performance characteristics. We gratefully acknowledge funding provided by the Office of Naval Research.

REFERENCES

- 1 E. G. Zaidman and M. A. Kodis, "Emission Gated Device Issues," IEEE Trans. Elec.Dev. **38**(10), 2221 (1991).
- 2 M. Garven, Ph.D. Thesis, University of Strathclyde, 1994.
- 3 A. V. Haeff and L. S. Nergaard, "A Wide-Band Inductive Output Amplifier," Proc. IRE, **28**, 126, March 1940.
- 4 A. V. Haeff, "An Ultra-High-Frequency Power Amplifier of Novel Design," Electronics, **12**, 30, March 1939.
- 5 R.I. Sarbacher and W.A. Edson, *Hyper- and Ultrahigh Frequency Engineering* (New York, John Wiley and Sons, 5th Ed) 1943.
- 6 A. J. Lichtenberg, "Prebunched Beam Traveling-Wave Tube Studies," IRE Trans. Elec. Dev. **ED-9**(4), pp. 345-351 (1962).
- 7 W. H. Smith and D. H. Leeds, "Pyrolytic Graphite," Modern Materials **7**, pp. 139-221 (1970).
- 8 W. F. Knippenberg, B. Lersmacher, H. Lydtin, and A. W. Moore, "Pyrolytic Graphite," Phillips Technical Review **28**(8), pp. 231-242 (1967).
- 9 W. F. Knippenberg, B. Lersmacher, and H. Lydtin, "Products of Pyrolytic Graphite," Phillips Technical Review **37**(8), pp. 189-196 (1977).

- 10 D. H. Preist and M. B. Shrader, "The Klystrode—An Unusual Transmitting Tube With Potential for UHF-TV," *Proc. IEEE* **20**(11), pp. 1318-1325 (1982).
- 11 M. B. Shrader and D. H. Preist, "Klystrode Update," Paper 29.3, Tech Digest IEDM, IEDM 84CH2099-0 (1984).
- 12 D. H. Priest and M. B. Shrader, "A High Power Klystrode with Potential for Space Application," *IEEE Trans. Electron Devices* **38**(10), pp. 2205-2211 (1991).
- 13 M. A. Kodis, H. P. Freund, N. R. Vanderplaats, and E. G. Zaidman, "Interaction Efficiency of an Emission Gated TWT," Tech Digest IEDM, pp. 589-591 (1991).
- 14 M. A. Kodis, N. R. Vanderplaats, E. G. Zaidman, B. Goplen, D. N. Smithe, and H. P. Freund, "Twystrode Experiments with Tapered and Untapered Helices," Tech Digest IEDM, pp. 795-798 (1994).
- 15 B. Goplen, D. N. Smithe, K. Nguyen, M. A. Kodis, and N. R. Vanderplaats, "MAGIC Simulations and Experimental Measurements from the Emission Gated Amplifier I & II Experiments," Tech Digest IEDM, pp. 759-762 (1992).
- 16 D. N. Smithe, B. Goplen, L. Ludeking, M. A. Kodis, and N. R. Vanderplaats, "Predicting Twystrode Performance," to be published.
- 17 K. L. Jensen and E. G. Zaidman, "Analytic Expressions for Emission Characteristics as a Function of Experimental Parameters in Sharp Field Emitter Devices," *J. Vac. Sci. Technol.* **B13**, 551 (1995).
- 18 E. G. Zaidman, "Simulation of Field Emission Microtriodes," *IEEE Trans. on Electron Devices* **40**, 1009 (1993).
- 19 D. W. Jenkins, "Emission Area of a Field Emitter Array," *IEEE-TED* **40**, 666 (1993).
- 20 D. Nicolaescu and V. Avramescu, "Field Emission Diode Characterization through Model Parameters Extraction from Current-Voltage Experimental Data," *J. Vac. Sci. Technol.* **B12**, 749 (1994).
- 21 D. Nicolaescu, "Physical Basis for Applying the Fowler-Nordheim J-E Relationship to Experimental I-V data," *J. Vac. Sci. Technol.* **B11**, 392 (1993).
- 22 D. A. Kirkpatrick, A. Mankofsky, and K. T. Tsang, "Analysis of Field-Emission from 3-Dimensional Structures," *App. Phys. Lett.* **60**, 2065 (1992).
- 23 K. L. Jensen, E. G. Zaidman, M. A. Kodis, B. Goplen, and D. N. Smithe, "Theory and Simulation of a Field Emission Microtriode: Analysis and Incorporation into Macroscopic Device Characterization," (unpublished).
- 24 K. L. Jensen and E. G. Zaidman, "Analytic Expressions for Emission Characteristics as a Function of Experimental Parameters in Sharp Field Emitter Devices," *J. Vac. Sci. Technol.* **B13.2** (1995) (in press).

- 25 A. Renau, F. H. Read, and J. N. H. Brunt, "The Charge-Density Method of Solving Electrostatic Problems With and Without the Inclusion of Space-Charge," *J. Phys. E: Sci. Instrum.* **15**, 347 (1982).
- 26 R. L. Hartman, W. A. Mackie, and P. R. Davis, "Use of Boundary Element Methods in Field Emission Computations," *J. Vac. Sci. Technol.* **B12**, 754 (1994).
- 27 K. L. Jensen, E. G. Zaidman, M. A. Kodis, B. Goplen, and D. N. Smithe, "Theory and Simulation of a Field Emission Microtriode: Analysis and Incorporation into Macroscopic Device Characterization," (unpublished).
- 28 K. Nguyen, L. Ludeking, G. Warren, and B. Goplen, "Analysis of the 425 MHz Klystrode," *IEEE Trans. Electron Devices*, **38**(10), (1991).
- 29 B. Goplen, L. Ludeking, D. Smithe, and G. Warren, "User-Configurable MAGIC Code for Electromagnetic PIC Calculations," *Computer Physics Communications* **87**(1)(2), pp. 54-86, (1995).
- 30 J. R. Pierce, *Travelling Wave Tubes* (Van Nostrand, Princeton, NJ, 1950), Chap. III and Appendix II.
- 31 D. Smithe, G. Warren, and B. Goplen, "A Helix Polarization Model for 2-D Particle-in-Cell Simulation of Helix Traveling Wave Tubes," 1992 APS Division of Plasma Physics Annual Meeting, *Bulletin of the American Physical Society*, **37**(6) (1992).
- 32 M. A. Kodis, N. R. Vanderplaats, H. P. Freund, B. Goplen, and D. N. Smithe, "Emission Gated Amplifier," 1993 APS Division of Plasma Physics Annual Meeting, *Bulletin of the American Physical Society* **38**(10), (1993).
- 33 B. Goplen, L. Ludeking, D. N. Smithe, M. A. Kodis, K. L. Jensen, and E. G. Zaidman, "Analysis of the Inductive Output Amplifier," (to be published).